



Preparation, characterization and microhardness measurements of hybrid nanocomposites based on PMMA + P(VDF–TrFE) and graphene oxide

Rohan Sagar¹ · M. S. Gaur¹ · Vinod Kushwah¹ · Aakash Rathore² · D. G. Piliptsov³ · A. A. Rogachev³

Received: 18 May 2020 / Revised: 14 September 2020 / Accepted: 1 November 2020 /
Published online: 19 November 2020
© Springer-Verlag GmbH Germany, part of Springer Nature 2020

Abstract

The polymer nanocomposites samples of the poly (methyl methacrylate) (PMMA)—poly (vinylidene fluoride–trifluoroethylene) P(VDF–TrFE) with graphene oxide (GO) were prepared by solution casting method. The impact of GO on electroactive polar β -phase of PMMA + P(VDF–TrFE) was investigated through the Fourier transform infrared spectroscopy (FTIR) and atomic force microscopy. The mechanical properties of nanocomposites samples have been investigated by measurement of microhardness. The value of microhardness and indentation depends on applied load on samples. The experimental result suggests that mechanical properties of samples decrease in presence of GO due to decrease in uniaxial orientation or agglomeration of GO. Surface characteristics such as surface free energy, interfacial free energy and hydrophobicity were determined by measuring the contact angle.

Keywords Graphene oxide · FTIR · AFM · Contact angles · Microhardness of thin films

Introduction

The combination of poly (methyl methacrylate) (PMMA) with poly (vinylidene fluoride–trifluoroethylene) P(VDF–TrFE) is a standout among the most promising ferroelectric polymers. The previous studied in these polymers have been

✉ M. S. Gaur
mulayamgaur@rediffmail.com

¹ Department of Physics, Hindustan College of Science and Technology (affiliated to Dr. A.P.J. Abdul Kalam Technical University, Lucknow, U.P. 226031, India), Farah, Mathura, Uttar Pradesh 281122, India

² Department of Mechanical Engineering, J.S.S. Academy of Technical Education, Noida, Uttar Pradesh 201301, India

³ Francisk Skorina Gomel State University, Gomel, Belarus

successfully demonstrated their non-volatile and low cost memory devices applications [1, 2]. The PMMA + P(VDF–TrFE) can crystallize in different phases (α and β) depending on the heating conditions. Among these two phases, the β -phase is found to have most noteworthy ferroelectric properties. Nonpolar α -phases of PMMA + P(VDF–TrFE) composite are often reborn into polar β -phase by stretching or by heat treatment [3]. The interface formed in blend and nanocomposites system plays an important role to modify electrical and mechanical properties of ferroelectric polymers [4–11].

The ferroelectric polymer P(VDF–TrFE) (vinylidene fluoride-co-trifluoroethylene) was chosen as the dielectric material for its extremely high permittivity. Linear PMMA polymer was introduced into P(VDF–TrFE) matrix in order to minimize the ferroelectric effect of P(VDF–TrFE) and thus increase the reversibility. In addition, dynamic hysteresis is also associated with the friction force between water droplets and the insulator surface [12, 13].

In recent years, micro- and nanoindentation have been established as a means of detecting a wide variety of mechanical, morphological and nanostructural changes in amorphous and semicrystalline polymers [14–35], including hybrids [16], copolymers [20, 36], polymer composites [19] and multilayer systems [15], however, no report is available in hybrid nanocomposites system of PMMA + P(VDF–TrFE) + GO. The precise mechanical properties of polymers and polymer nanocomposites cannot be easily determined because, so far, there is no comprehensive visco-elasto-plastic theory to account for their micromechanical properties. However, valuable attempts have been made in the past to explain the mechanical behavior of materials that do not exhibit fully plastic behavior [37, 38].

The novelty of this work lies in the new properties arising from the combination of two polymers with GO and different dispersion characteristics, which have not been reported previously [39, 40]. The graphene oxide is important filler in polymer matrix because nanocomposites have stemmed from their high surface area and mechanical stability [41]. Consequently, studying the mechanical properties of PMMA + P(VDF–TrFE) + GO hybrid nanocomposites brings a great interest as the researchers are trying to find an answer to the question: how can hybrid nanocomposites system change to pave the way for new practical applications [42, 43].

Synthesis of graphene oxide (GO) is achieved by placing graphite in concentrated acid in the presence of an oxidizing agent. The Tour method demonstrated a less hazardous and more efficient method for graphite oxidation. This method and its modified versions are presently the most commonly used methods for the oxidation of graphite [44, 45].

Graphene oxide (GO) is one of those materials—it is a single-atomic layered material, made by the powerful oxidation of graphite, which is cheap and abundant. Graphene oxide is an oxidized form of graphene, laced with oxygen-containing groups [46].

The mechanical properties of several polymers are strongly influenced by GO because of its good dispersion and good interaction with main chain of many polymers. Nevertheless, very high dispersion of GO is difficult to reach after a certain amount of loading above which it adversely affects modulus, strength and surface wettability of polymer nanocomposites. The GO finally affected the pore structure,

surface roughness and surface wettability of the polymer, which in turn is correlated with the mechanical properties of polymers [47–52].

The various mechanical properties varied with variation in applied load. Generally, there are two types of load (1) static load and (2) dynamic load. The applied load is the main parameter for testing of mechanical properties. For example, fatigue toughness is one of the most important properties of materials which can be determined by the behavior of the material under applied variable load. Various other material properties such as tensile strength, fracture toughness, toughness, ductility, elastic modulus and microhardness are investigated under application of static load [53–55].

In this paper, we report a study on GO-modified microhardness of PMMA + P(VDF–TrFE) hybrid nanocomposites samples. FTIR, AFM, contact angle measurement studies have been made to characterize the structural and surface properties of hybrid nanocomposites.

Experimental details

Materials

P(VDF–TrFE) ($M_w \sim 146.06 \text{ g mol}^{-1}$), PMMA ($M_w \sim 100.12 \text{ g mol}^{-1}$) and graphite powder ($M_w \sim 1201.6 \text{ g mol}^{-1}$) were purchased from Sigma-Aldrich. Sulfuric acid (H_2SO_4), sodium nitrate (NaNO_3), hydrogen peroxide (H_2O_2), hydrochloric acid (HCL) and potassium permanganate (KMnO_4) were procured from Sigma-Aldrich. Acetone, distilled water (DW) and *N, N*-dimethylformamide (DMF) were used as a solvent for preparation of hybrid nanocomposite thin film.

Fabrication of GO and PMMA + P(VDF–TrFE) hybrid nanocomposites

Graphene oxide (GO) was prepared by modified Hummer's method [56]. In this method, 0.5 g of graphite powder and 0.5 g NaNO_3 were mixed with 25 ml of concentrated H_2SO_4 . The mixture was continuously stirred for 30 min at the temperature range of 0–5 °C. Thereafter, 3 g of KMnO_4 flakes were slowly added to the suspension and the temperature was maintained below 25 °C under stirring, until this solution becomes light brownish. This solution was added with 45 ml of distilled water (DW) and 5 ml of H_2O_2 to reduce the excess of KMnO_4 . It was then sonicated for 24 h. The dark suspension was then centrifuged to remove ionic contaminants for 15 min at 10,000 rpm. The whole reaction mixture was washed by 1 M HCl and ethanol for 3–4 times and filtered to get the gray color of GO separate sheets in oxidized state. The GO was dried in the form of precipitate to stay away from aggregation. For the preparation of blend sample, different weight % of P(VDF–TrFE) was added with PMMA. We have optimized the wt% of GO in PMMA + P(VDF–TrFE) matrix and observed that 2 wt% of GO is the best choice to enhance morphological and mechanical properties.

We have prepared the 50- μm -thick nanocomposite thin films of PMMA + P(VDF–TrFE) with GO by using solution casting method. In this method,

polymer powder of (PMMA + P(VDF–TrFE)) with ratio of 80:20 was added in 50 ml of DMF and kept in stirrer for 2 h at 45 °C. Again we have added dried graphene oxide and stirred magnetically for 1 h at 45 °C. The solution was subjected to ultrasonic vibration for 20 min and stirred again for 6 h at 45 °C for a homogeneous distribution of GO. The resultant solution was poured in optically plane glass plate inside vacuum oven. The samples were kept at 60 °C inside vacuum oven for 24 h to remove the effect of all volatile contents before use.

Mechanism

The concentration fluctuation of PMMA and P(VDF–TrFE) around GO will disturb homogeneous entanglements of hybrid samples. Especially, GO strongly interacts with polymer due to the largest surface area.

The GO will act as entanglement points in hybrid sample and its density increases with increasing concentration, finally leading to the enhancement of phase stability [49].

The polar C–O–C and C=O groups of PMMA interact with strong polar fluoride groups of P(VDF–TrFE) (Fig. 1). The PMMA segment in nanocomposite film suppresses the free volume (or defect) existing in the normal P(VDF–TrFE) copolymers due to decrease in crystallinity and crystal size. The resultant properties of polymer GO hybrid nanocomposites depend on the intrinsic characters of GO (i.e., size). The functional groups, –OH and –COOH, exist on the surface and pores of the GO which promote the hydrogen bonds between the GO to amine, benzenoid and quinoid of the polymer chain [57, 58].

Results and discussion

P(VDF–TrFE) and PMMA are known to polar polymer and having excellent miscibility in common solvent. The addition of PMMA affected the crystallinity of P(VDF–TrFE), including the dilution and impeding the influence on the overall

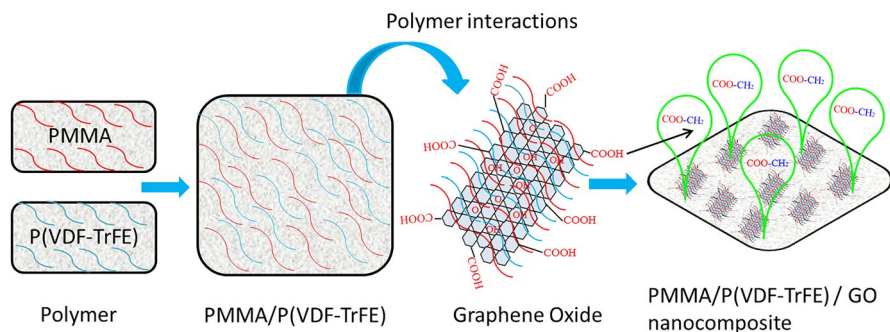


Fig. 1 Schematic diagram of polymer chain interactions with graphene oxide among polar groups of hybrid nanocomposites

crystallization of ferroelectric phase. The van der Waals forces and dipolar interactions strengthened the interfacial interactions. There are the van der Waals forces between the layers that can induce particle agglomeration, which will negatively affect the desirable properties [59]. The nanofiller aggregation means less surface contact between the polymers and GO consequently the polymer chains are free to move. The rigidity of PMMA + P(VDF–TrFE) and defects induced by GO agglomeration is responsible for measured microhardness. The tensile strength is strongly influenced by interfacial defects which lead to structure collapses. The GO and polymer have different surface energy; it causes agglomeration of GO in polymer matrix. This difference in surface energy could be minimized by proper sonication of solution or by using any inorganic chemical binder.

FTIR spectroscopy

Figure 2 shows the FTIR vibrational spectra of PMMA + P(VDF–TrFE) hybrid samples from 400 to 3600 cm^{-1} . The position of different functional groups of pristine and hybrid nanocomposites samples is given in Table 1.

The characteristic absorption bands of α -phase are observed at 482, 1175, 1271 and 1725 cm^{-1} , while characteristic absorption bands of β -phase are observed at 507, 658, 841 and 1436 cm^{-1} for pure P(VDF–TrFE) [60, 61] as shown in Fig. 2. The vibrational band at 507 cm^{-1} corresponds to bending vibrations mode of CF_2

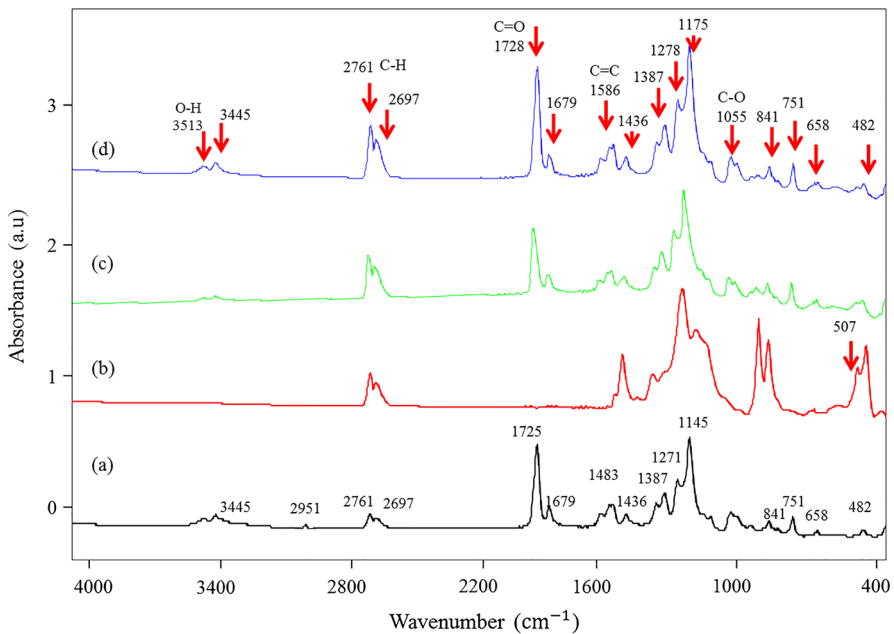


Fig. 2 FTIR spectrum of the **a** PMMA, **b** P(VDF–TrFE), **c** PMMA + P(VDF–TrFE) and **d** PMMA + P(VDF–TrFE) + 2 wt% GO for hybrid nanocomposites

Table 1 Characteristic of FTIR absorption for hybrid nanocomposites

Samples	Peak position (cm ⁻¹)	Phase	Assignment
PMMA	751		Wagging deformation (-CH ₃)
	989		Bending (CH ₃ -O)
	1192		Skeletal chain
	1251		Stretching deformation (C=O)
	1435		Stretching (CH ₂) and stretching, asymmetric(O-CH ₃)
	1482		Bending asymmetric (CH ₂)
	1712		Stretching (C=O)
	2951		ν_s (CH ₂) vibration asymmetric
	3445		O-H symmetric, hydroxyl group
	P(VDF-TrFE)	482	α
507		β	CF ₂ bending
841		β	CH ₂ rocking and CF ₂ asymmetric stretching
875		γ	CF ₂ symmetric stretching
1175		α	CH ₂ wagging deformation
1271		α	CF ₂ symmetric stretching
1436		β	CH ₂ wagging deformation
1725		α	CF out of plane deformation
PMMA + P(VDF-TrFE)	658	β	CF ₂ bending and wagging
	1387		C-H stretching
	1679		Stretching vibration peaks of (C=C) groups
	2761		C-H stretching symmetric
	2697		C-H stretching
PMMA + P(VDF-TrFE) + 2 wt% GO	1055		C-O stretching bond
	1586		C=C stretching
	1728		C=O stretching
	3513		O-H symmetric, intermolecular bonded

dipoles and characteristic of TT (trans) conformation of the ferroelectric β -phase of P(VDF-TrFE). The O-CH₃ bending and stretching of PMMA are assigned to vibrational bands at 987 and 1483 cm⁻¹. The stretching frequency of C=O band corresponds to 1679 and 1271 cm⁻¹. Absorption band at 841 cm⁻¹ shows the characteristic frequency of vinylidene compound. Stretching frequency at 1679 cm⁻¹ is shifted to 1725 cm⁻¹ which corresponds to C=O band of PMMA, in the hybrids (i.e., PMMA + P(VDF-TrFE) sample). This shift is due to carbonyl stretching frequencies of hybrids. This is also caused by specific interaction between the carbonyl groups of PMMA and the CH₂ groups of P(VDF-TrFE) which indicates the formation of hybrids. The results are supported by the analysis of PMMA + P(VDF-TrFE) hybrid by Coleman et al. [62]. We have investigated the influence of PMMA chains on formation of crystalline β -phase of P(VDF-TrFE). We found that the intensity of

841 cm^{-1} band is the function of PMMA and GO content. For example, intensity of PMMA + P(VDF–TrFE) hybrid at 841 cm^{-1} band decreases, when 2 wt.% of GO is added.

Figure 2 shows the FTIR characteristics of PMMA, P(VDF–TrFE), PMMA + P(VDF–TrFE) and 2 wt% GO contents samples. The P(VDF–TrFE) sample presents α -phase absorptions peak at 482, 1175 and 1271 cm^{-1} . It is clear from Fig. 2(b) that P(VDF–TrFE) sample exhibits nonpolar α -phase. FTIR results show that all absorption bands of the α -phase disappear, while new absorption bands at 841, 1271 and 1387 cm^{-1} have been observed, implying the transformation of the nonpolar α -phase to both electroactive β - and γ -phases [63, 64]. However, several absorption bands of pure PMMA at 841 and 1271 cm^{-1} are nearly according with these characteristic absorptions at 838, 1145 and 1271 cm^{-1} and disturb our judgment of whether electroactive β - and γ -phases do exist [65, 66]. Considering FTIR results, it is reasonable to understand that addition of PMMA transforms nonpolar α -phase to electroactive β - and γ -phases, but introduction of GO into PMMA + P(VDF–TrFE) hybrid sample gives the further change in FTIR spectra. In the FTIR spectra of P(VDF–TrFE) + PMMA + GO hybrid nanocomposites, though absorptions at 838 and 1271 cm^{-1} still exist, the absorption of the β -phase at 1278 cm^{-1} is hard to observe, which indicates that GO addition further induces electroactive γ -phase dominant phase structure.

The bands of PMMA + P(VDF–TrFE) + GO at 2995 cm^{-1} and 2951 cm^{-1} represent the asymmetrical and symmetric stretching of CH_2 , respectively. The presence of different oxygen functionalities in the graphene oxide was confirmed at 3513 cm^{-1} (O–H stretching). The FTIR results confirm with XRD results by exposing the same phenomenon for electroactive β -phase intensity variation with the GO concentration and show a linear increasing trend up to 2 wt% GO within PMMA + P(VDF–TrFE) polymer matrix [67].

Atomic force microscopy

The grain size, particle size and roughness of the film (~ 32.21 nm, 79.65 nm and 41.02 nm), respectively, for 2 wt% GO of PMMA + P(VDF–TrFE) hybrid nanocomposite film were estimated by using AFM. The particle distribution and surface 2D topography images are shown in Fig. 3a–d. AFM demonstrates the structural morphology of PMMA + P(VDF–TrFE) + 2 wt% GO. In addition to that, a new observation is seen, i.e., at the surface of thin films, GO particles are present having size less than 2 μm . Roughness and average grain size are found to be increased for PMMA + P(VDF–TrFE) + GO hybrid nanocomposites. The RMS roughness and average grain size of GO and its hybrid nanocomposite were found to be 41.02 and 32.21 nm, respectively.

The topography AFM images for all samples in the contact mode are displayed in Fig. 3(a–d) which shows the topography of surface PMMA, P(VDF–TrFE), PMMA + P(VDF–TrFE) and PMMA + P(VDF–TrFE) + GO hybrid nanocomposite samples. P(VDF–TrFE) sample of this type of structure differs from hybrid nanocomposites. The detailed heights along with the yellow

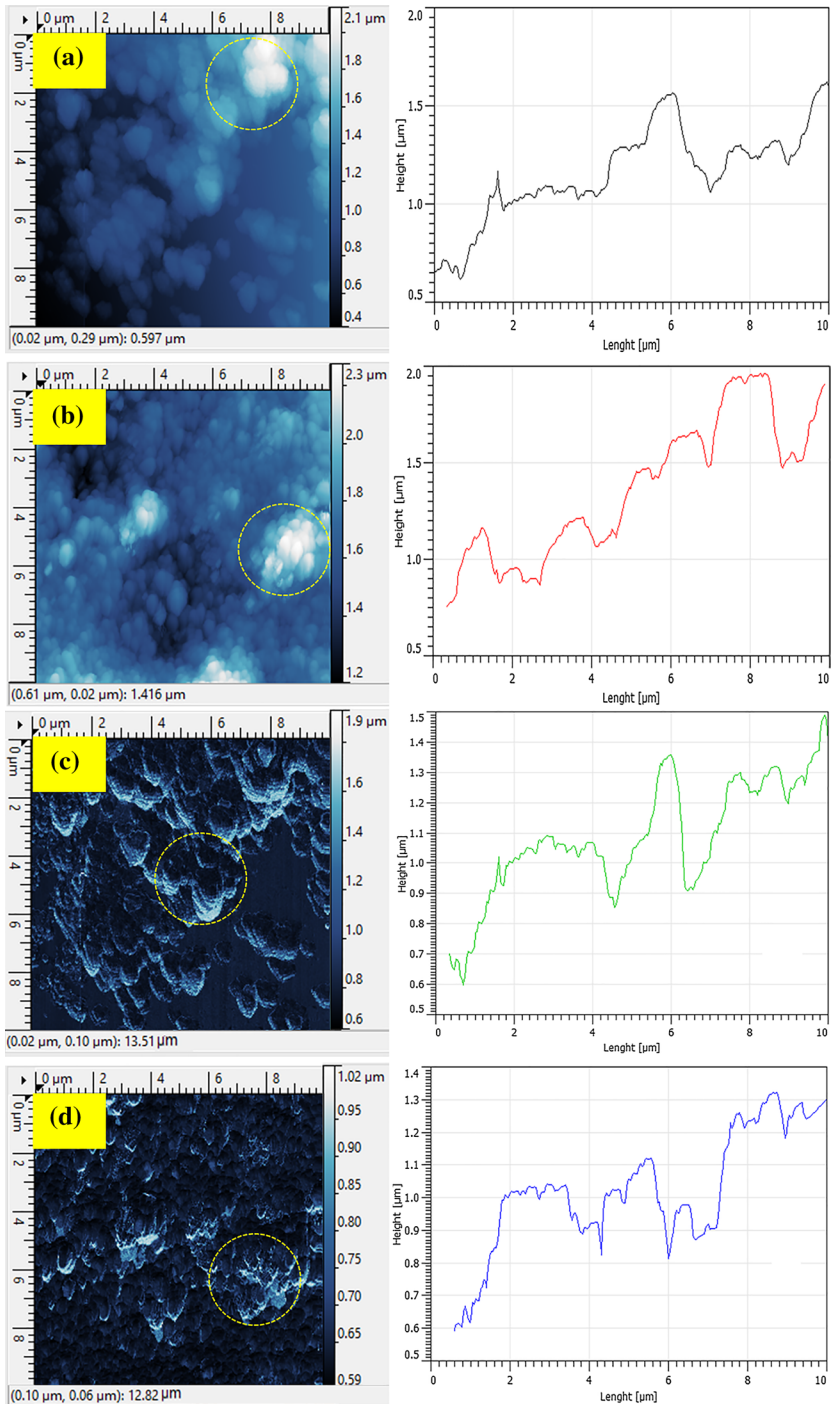


Fig. 3 AFM 2D images of the **a** PMMA, **b** P(VDF-TrFE), **c** PMMA+P(VDF-TrFE) and **d** PMMA+P(VDF-TrFE)+2 wt% GO for hybrid nanocomposites

dotted circle of Fig. 3a–d are shown by the right sided height curve. The roughness of P(VDF–TrFE) and PMMA sample is 44.11 and 48.02 nm, respectively. The roughness of hybrid sample significantly enhances as shown in Fig. 3c, while roughness of PMMA + P(VDF–TrFE) + GO hybrid nanocomposites decreases (i.e., Fig. 3d). Figure 3 shows the several wide and lofty peaks, manifesting the current aggregation of large grains. The microhardness of material is the function of grain size. AFM images are characterized by separate lamellar crystallites have different grain size, which affects the microhardness.

AFM recognizes two phases (i.e., hard and soft phase) in 3D images. Microhardness results support the hybrid nanocomposites, which are more crystalline as well as hard in comparison with pristine system and finally exhibit mostly hard phases as shown in Fig. 4a–b. The PMMA and P(VDF–TrFE) samples have hard phases with higher value of surface roughness. However, surface roughness of hybrid sample decreases in presence of GO.

Structural changes in hybrid nanocomposite samples are caused by change in sizes of lamellar crystal by introducing GO in polymer matrix. AFM also illustrates the surface morphology of PMMA, P(VDF–TrFE) and PMMA + P(VDF–TrFE) + GO hybrid nanocomposite samples. The P(VDF–TrFE) images display small voids in the interconnected morphology. The 2D and 3D images of AFM represent the reduction in microvoids with 2 wt% of GO, which corresponds to a reduction in surface roughness as shown in Table 2. The surface roughness is observed to be lower for lower concentration of 2 wt% GO in PMMA + P(VDF–TrFE) hybrid nanocomposites. The decrease in void size in nanocomposite samples represents uniform dispersion of GO. This finally causes the reduction in particle size and grain size as shown in Table 2. In a nanocomposites sample, the particle size is macrophenomenon, while grain size is

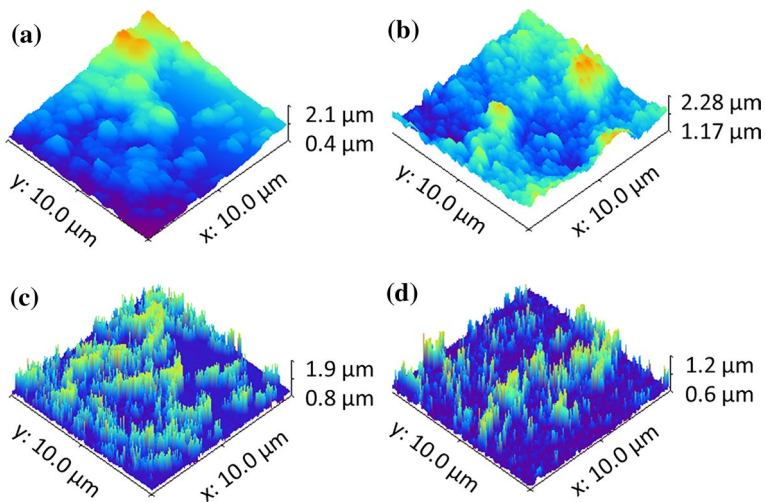


Fig. 4 AFM 3D images of the **a** PMMA, **b** P(VDF–TrFE), **c** PMMA + P(VDF–TrFE) and **d** PMMA + P(VDF–TrFE) + 2 wt% GO for hybrid nanocomposites

Table 2 AFM parameters of hybrid nanocomposites

Samples	Particle size(nm)	Average grain size (nm)	Average roughness size (nm)
PMMA	86.52	80.40	48.02
P(VDF–TrFE)	58.26	53.18	44.11
PMMA + P(VDF–TrFE)	90.91	26.72	53.17
PMMA + P(VDF–TrFE) + 2 wt% GO	79.65	32.21	41.02

microphenomenon. In the present study, grain size was in the range of 48 nm. This range of grain size occurs due to the quantum effect [68–70].

Microhardness and tensile strength

The measurement of the microhardness variation at room temperature is subjected to volume fraction of spherulites during primary crystallization of a number of polymer materials [71–73]. The following equation relates the microhardness parameters of polymers:

$$H = H_{\text{sph}}\phi + H_{\text{a}}(1 - \phi) \quad (1)$$

where H_{sph} and H_{a} are the microhardness values of the spherulitic and the amorphous inter-spherulitic regions in polymer, respectively. In general, microhardness values during primary crystallization are shown to be directly proportional to the total emerging crystallinity in the sample [74, 75]. It arises from the direct proportionality between the microhardness of the spherulites and the fraction of crystalline material within them (i.e., α_{L}) [71, 76, 77]:

$$H_{\text{sph}} = H_{\alpha_{\text{L}}} + H_{\text{a}}(1 - \alpha_{\text{L}}) \quad (2)$$

Combination of Eqs. (1 and 2) yields:

$$H = H_{\alpha} + H_{\text{a}}(1 - \alpha) \quad (3)$$

It is reported that the microhardness and other mechanical properties of polymers are enhanced with carbonaceous nanofiller, however, it is not necessary for electrical properties of GO based polymer nanocomposites [78, 79].

The decrease in microhardness of PMMA + P(VDF–TrFE) + GO hybrid nanocomposites is due to less uniaxial orientation of GO or aggregation of GO. The GO exhibits hydroxyl, carboxyl and carbonyl oxygen-containing functional groups, which are hydrophilic and highly reactive nano-reinforcements in aqueous system. The decrease in microhardness of GO nanocomposites sample as compared to pure PMMA and PMMA + P(VDF–TrFE) hybrid is due to uniaxial orientation of GO [80, 81].

Microhardness test is developed to measure the microhardness of materials. It can be used for all materials and has one of the broadest scales among microhardness tests. Microhardness is determined when force is applied by an indenter to

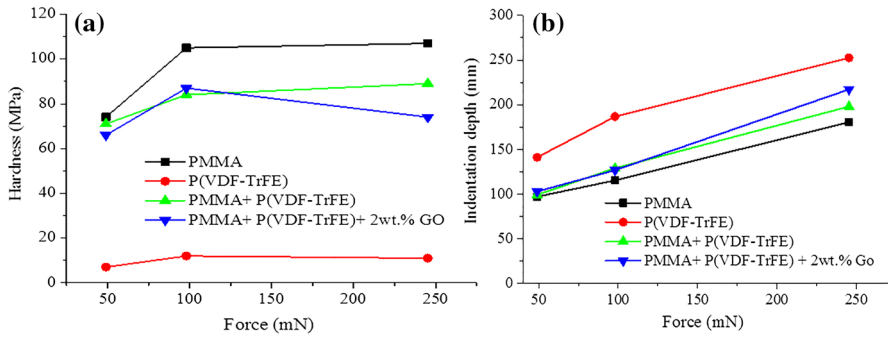


Fig. 5 The variations in force **a** microhardness at room temperature and **b** force–displacement curves of indentation depth for hybrid nanocomposites

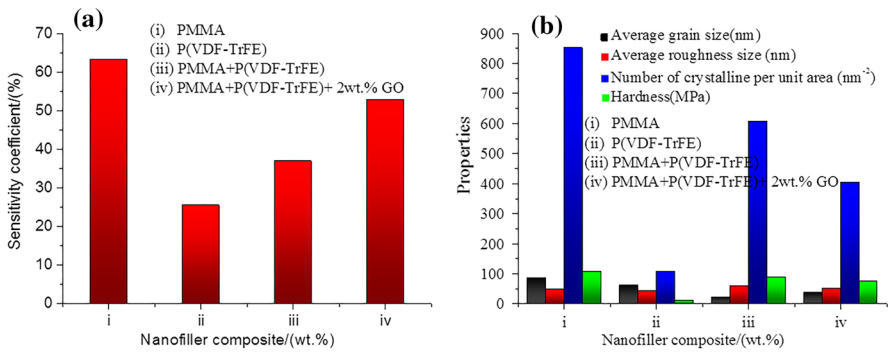


Fig. 6 Effect of nanofiller on, **a** sensitivity coefficients and **b** related properties of hybrid nanocomposites

the surface of samples. In this study, the mechanical characterizations of nanocomposites materials are performed using AFFRI brand DM-8 motorized digital microhardness tester. The microhardness values (H) of different applied loads are in the range of 49.03–245.2 Nm. This was calculated by using Eqs. 4 and 5 [82]. F is the load applied in sample surface, A is the micrometer square surface area and d is the indented edge length.

$$H = \frac{F}{A} \tag{4}$$

$$H = 14.22F/d^2 \tag{5}$$

The load-dependent microhardness and indentation depth are shown in Fig. 5a–b. Figure 6a–b shows representative load displacement curves from nanoindentation measurement performed on PMMA + P(VDF–TrFE) + GO hybrid nanocomposites. The standard Oliver and Pharr method was used for the analysis of microhardness (H), yield strength (Y_s), average grain size (G_a),

average roughness (R_a), tensile strength (T_s) and number of crystalline per unit area (N) [83–86]. These parameters are presented in Table 3.

The indentation depths of less than 250 nm (245 mN) are observed in load–displacement curve. Figure 5a shows linear elastic (reversible) loading and unloading behaviour of load–displacement curve. It is due to fact that indentation at lower value of load did not prove the damage of polymer surface.

Figure 5a reveals that the microhardness is maximum at 100 mN force for all samples, however, PMMA shows maximum value of microhardness. After 100 mN force, the microhardness is gradually decreased.

The microhardness of polymer nanocomposites depends on the nature of polymer nanofiller interface. The microhardness will increase, if nanofiller concentrates on the interface due to good interface adhesion, however, microhardness decreases due to poor interface adhesion. The decrease in microhardness in hybrid nanocomposites samples with GO is probably due to uniaxial orientation of GO or agglomeration of the GO in polymer matrix [87, 88]. The agglomeration of GO is discarded from AFM study, therefore, uniaxial orientation of GO is the only reason for decrease in microhardness.

The indentation depth of P(VDF–TrFE) is the highest as compared to PMMA, PMMA + P(VDF–TrFE) and PMMA + P(VDF–TrFE) + GO samples. We have observed that the addition of GO in PMMA + P(VDF–TrFE) composite slightly decreases the indentation depth in general. It is due to fact that the plastic deformation of PMMA + P(VDF–TrFE) is controlled by GO.

Tensile and yield strengths were computed from the following relation [89, 90]:

$$T_s = -99.8 + 3.734H \quad (6)$$

$$Y_s = -90.7 + 2.876H \quad (7)$$

where T_s tensile strength, Y_s yield strength and H microhardness.

The microhardness parameters of PMMA, P(VDF–TrFE), PMMA + P(VDF–TrFE) and PMMA + P(VDF–TrFE) + 2 wt% GO samples are shown in Table 3. The addition of GO in PMMA + P(VDF–TrFE) reduces the T_s due to its uniaxial orientation. The tensile strength values of P(VDF–TrFE) decreases with combination of PMMA and GO. The P(VDF–TrFE) showed the lowest yield strength and its Y_s increases with combination of PMMA/GO due to brittle essence of PMMA [91].

It is seen that tensile and yield strengths are negatively correlated with average grain size and surface roughness, whereas they are positively correlated with the number of crystalline or number of particle per unit area (i.e., Table 3).

The P(VDF–TrFE) is a crystalline as well as amorphous polymer. P(VDF–TrFE) is the copolymers of PVDF that have offered a straight forward approach to obtaining the electroactive phase due to presence of pores. Consequently, it will decrease the mechanical properties [92–94].

In the present study, the nanoindentation measurements are also correlated with AFM images (Fig. 2a–d) due to similar surface profile of all samples after nanoindentation. The GO is harder than PMMA + P(VDF–TrFE) in

Table 3 Microhardness parameters of hybrid nanocomposites

Samples	F (mN)	H (MPa)	Y_s (N mm ⁻²)	T_s (N mm ⁻²)	G_a (nm)	R_a (nm)	(N) (1 mm ⁻²)
PMMA	245	107	217	299.7	86	47	851.6
P(VDF-TrFE)	245	11	59	232.5	61	43	107.2
PMMA + P(VDF-TrFE)	245	89	165.2	158.7	22	59	607.7
PMMA + P(VDF-TrFE) + 2 wt% GO	245	74	122.2	176.5	38	51	404.4

Microhardness (H), Applied load (F), Yield strength (Y_s), Average grain size (G_a), Average Roughness (R_a), Tensile strength (T_s) and Number of crystalline per unit area (N)

nanocomposites samples, hence during indentation run, if indenter falls in the nanocomposites matrix, where GO is present, the depth of indentation would reduce significantly and there would be an increase in surface deformation around the region.

Sensitivity coefficient

The several parameters such as force, diameter/thickness of sample and depth are affecting the microhardness of sample. They are also responsible for uncertainty on measurement. The uncertainty in measurement is given by following relation [86]:

$$c = \frac{\Delta H}{\Delta x} \quad (8)$$

where Δx is the input parameter that has been changed (load) and ΔH is the change in microhardness. The sensitivity coefficient represents accuracy of microhardness measurement. The sensitivity coefficients (c) can be analyzed from microhardness measurements. For sensitivity analysis, we observed that the sensitivity of PMMA is more than P(VDF–TrFE) and PMMA + P(VDF–TrFE) and PMMA + P(VDF–TrFE) + GO samples as shown in Fig. 6a.

Contact angles

The contact angle for PMMA, P(VDF–TrFE), PMMA + P(VDF–TrFE), PMMA + P(VDF–TrFE) + GO samples with respect to water and glycerin has been measured by very simple sessile drop method [95].

The surface energy associated with polymer nanocomposites samples with respect to water and glycerin was determined by measuring contact angle. It is reported in the literature [96] that PMMA is more hydrophobic than P(VDF–TrFE). The mixing of P(VDF–TrFE) in PMMA matrix will significantly affect the hydrophobicity of PMMA. The surface of the PMMA + P(VDF–TrFE) + GO hybrid nanocomposites contains some of the GO particles and this eventually decreased the hydrophobic nature. It could be clearly seen in Fig. 7a–d by variation in contact angle.

It is clearly observed that contact angles for PMMA + P(VDF–TrFE) + GO samples with respect to water and glycerin are 79.24°, 83.08°, 62.30°, 81.20° and 69.55°, 81.64°, 61.36°, 75.27°, respectively, as shown in Fig. 8a. The forces acting on surface of the PMMA + P(VDF–TrFE) and PMMA + P(VDF–TrFE) + GO samples are vanished as compared to pristine sample of PMMA and PMMA + P(VDF–TrFE) samples due to polar nature of water and glycerine. Therefore, surface free energy decreases at the surface of PMMA + P(VDF–TrFE) and PMMA + P(VDF–TrFE) + GO samples.

The contact angles were measured in four different places of sample with 1 μ l of liquid. Owens and Wendt equation [97, 98] was used to calculate the solid surface energy:

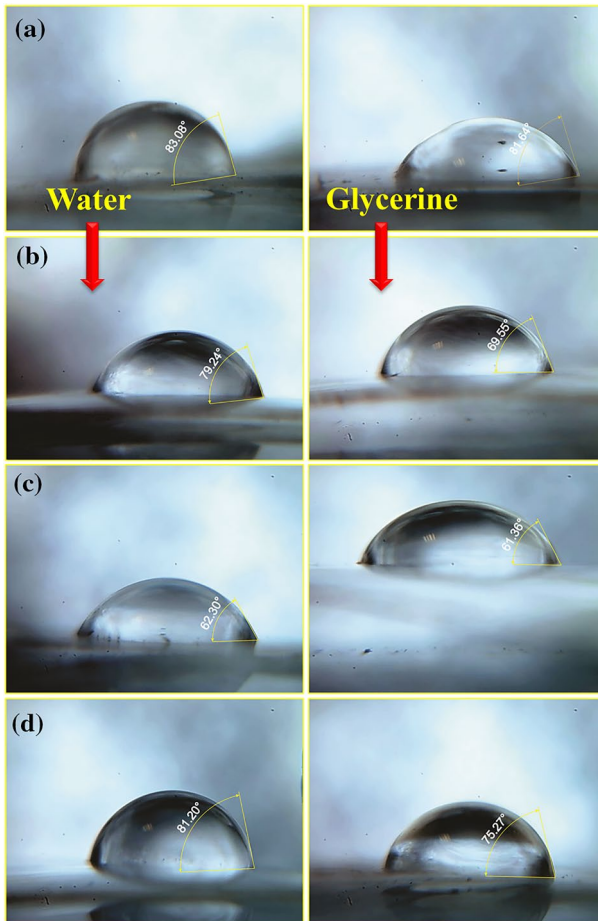


Fig. 7 Contact angle images of the **a** PMMA, **b** P(VDF-TrFE), **c** PMMA+P(VDF-TrFE) and **d** PMMA +P(VDF-TrFE) + 2 wt% GO for hybrid nanocomposites

$$\cos \theta = \left[2\sqrt{\gamma_s^d} \left(\frac{\sqrt{\gamma_L^d}}{\gamma_L} \right) + 2\sqrt{\gamma_s^p} \left(\frac{\sqrt{\gamma_L^p}}{\gamma_L} \right) - 1 \right] \tag{9}$$

where θ is the contact angle, γ_s and γ_L are the solid and liquid surface energy, respectively. γ_s^d and γ_s^p are dispersion forces and polar forces of total surface energy ($\gamma = \gamma_s^d + \gamma_s^p$).

The surface energy with respect to polar liquid in polymer is caused by interaction of polar molecules with solid surface that has permanent dipole moment. However, dispersive part is originated due to random fluctuations in the electron density when solid and liquid interacted together.

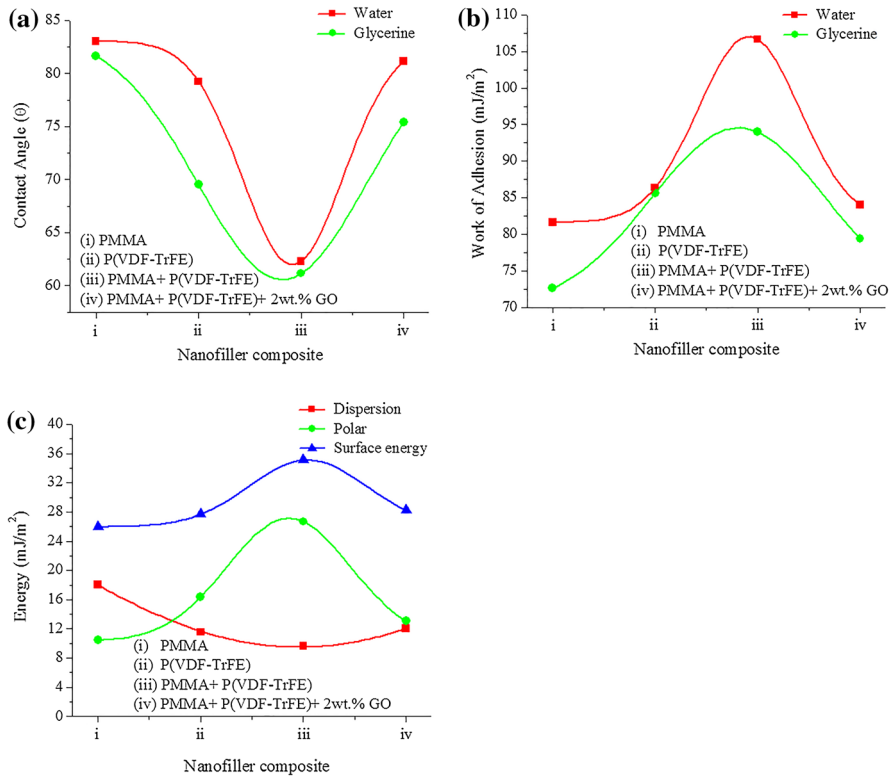


Fig. 8 The effect of nanofiller composite **a** contact angle, **b** work of adhesion and **c** surface energy for hybrid nanocomposites

The measurement of contact angle of polymer nanocomposites with two kinds of liquids with known surface energy components, γ_s^d and γ_s^p explained by Rohan et. al [99].

The calculated value of surface energy for PMMA-based nanocomposites samples is presented in Table 4. The surface energy of PMMA is increased from 26.04 to 35.46 $mJ m^{-2}$ when P(VDF-TrFE) is added. However, hydrophilicity of PMMA is related to the contributions of dipole–dipole and dipole–induced dipole interactions.

Table 4 Contact angle (θ) of work of adhesion (W_A) and surface energy (γ_s) of hybrid nanocomposites

Samples	(θ)		(W_A) ($mJ m^{-2}$)		(γ_s) ($mJ m^{-2}$)
	Water	Glycerine	Water	Glycerine	
PMMA	83.08	81.64	81.62	72.61	26.04
P(VDF-TrFE)	79.24	69.55	86.38	85.58	27.62
PMMA + P(VDF-TrFE)	62.30	61.36	106.65	93.98	35.46
PMMA + P(VDF-TrFE) + 2 wt% GO	81.20	75.27	84.01	79.35	28.47

Also, the contact angle and adhesion work for PMMA + P(VDF–TrFE) + 2 wt% GO hybrid nanocomposites are affected by the water. The surface roughness and molecular interactions are the main reasons for these results shown in Fig. 8(b).

The weak interaction of $-\text{CF}_2$ groups of P(VDF–TrFE) is the reason of its weak hydrophobicity [95]. The PMMA and PVDF have almost similar dispersion component (γ_s^d), but addition of P(VDF–TrFE) in PMMA enhances the polar component (γ_s^p) and finally increases the surface energy of nanocomposites as presented in Fig. 8(c). It has been observed that the surface composition of PMMA + P(VDF–TrFE) + GO sample was highly influenced by GO, which reflects the variation in surface energy.

Generally, the crystalline nuclei are formed at the end of the polymer chain, and size of the nuclei is independent on isolated amorphous chains of polymer like PMMA. Table 3 shows that the crystallinity of PMMA is greater than crystallinity of P(VDF–TrFE), however, PMMA + P(VDF–TrFE) + GO hybrid nanocomposites have higher crystalline than the P(VDF–TrFE) and less crystalline than PMMA. It may be due to agglomeration of GO being able to reduce the electrostatic force between the hybrid polymer matrix and the graphene oxide, which is responsible for reduction in crystallinity of the hybrid nanocomposites (Fig. 6b) [100, 101].

Thus, hydrophilicity of individual and composite samples is affected the microhardness, surface enrichment and crystallization. Factors affecting the surface hydrophilicity of polymer nanocomposites are reported in the literature [98]. In general, the hydrophilicity of polymer is the part of (i) crystallization domains contraction on the sample surface and (ii) surface enrichment tendency of polymer. The literature [102] demonstrates that contact angle measurement provides the information about level of intercalation between nanofiller and the polymer.

The decrease in contact angle is subjected to increase in nanofiller concentration. This means that intercalation between nanofiller and polymer enhances. It has been verified by AFM technique.

Conclusions

FTIR and AFM characterization results confirm the formation of hybrid nanocomposite of PMMA with P(VDF–TrFE) and GO. The contact angle measurement confirms the intercalation of GO with polymer matrix and its hydrophobic properties.

In summary, we have emphasized attractive applications of the microindentation method to the study of the mechanical properties of polymer nanocomposites surfaces. The isolated microhardness (H) of value up to 107 MPa could be easily scaled down to develop submicron level uniform small crystal of P(VDF–TrFE). In addition, the surface structural analysis of polymer/hybrid nanocomposites samples by AFM technique and contact angle measurement supports the results of mechanical properties by means of uniaxial orientation of GO and its dispersion in polymer matrix. The improvement in microhardness and yield strength of hybrid nanocomposites is found to mainly depend on the concentration of GO in polymer interface adhesion. It is concluded that our attempt of this study will help to understand the fundamental concept of “nano” effect in polymer, liquid–solid interaction in hybrid

nanocomposites system by measuring contact angle and pave the way for industrial applications in several flexible electronic devices.

Acknowledgements This work was financially supported by Indo-Belarusian Scientific Cooperation, DST, New Delhi (India) (Letter No.INT/BLR/P-13/2016) which is gratefully acknowledged. One of the authors Rohan Sagar acknowledges the University Grant commission (UGC), New Delhi (India) for providing research fellowship award number (RGNF-2017-18-SC-UTT-29088).

References

1. Reece TJ, Ducharme S, Sorokin AV, Poulsen M (2003) Nonvolatile memory element based on a ferroelectric polymer Langmuir–Blodgett film. *Appl Phys Lett* 82:142–144
2. Naber RCG, Tanase C, Blom PWM, Gelinck GH, Marsman AW, Touwslager FJ, Setayesh S, de Leeuw DM (2005) High-performance solution-processed polymer ferroelectric field-effect transistors. *Nat Mater* 4:243–248
3. Mir SH, Hasan PMZ, Danish EY, Aslam M (2020) Pd-induced phase separation in poly (methyl methacrylate) terpolymer: synthesis of nanostructured catalytic Pd nanorods. *Colloid Polym Sci* 298:441–448
4. Fujisaki S, Ishiura H, Fujisaki Y (2007) Poly (vinylidene fluoride–trifluoroethylene)/barium titanate nanocomposite for ferroelectric nonvolatile memory devices. *Appl Phys Lett* 90:162–192
5. Salimi A, Yousef AA (2004) Conformational changes and phase transformation mechanisms in PVDF solution-cast films. *J Polym Sci Part B Polym Phys* 42:3487–3495
6. Naber RCG, Blom PWM, Marsman AW, de Leeuw DM (2004) Low voltage switching of a spin cast ferroelectric polymer. *Appl Phys Lett* 85:2032–2034
7. Noda K, Ishida K, Kubono A, Horiuchi T, Yamada H, Matsushige K (2003) Remanent polarization of evaporated films of vinylidene fluoride oligomers. *J Appl Phys* 93:2866–2870
8. Xia F, Xu HH, Razavi B, Cheng Z-Y, Zhang QM (2002) Dependence of threshold thickness of crystallization and film morphology on film processing conditions in poly(vinylidene fluoride–trifluoroethylene) copolymer thin films. *J Appl Phys* 92(6):3111–3115
9. Xia F, Xu H, Fang F, Razavi B, Cheng Z-Y, Lu Y, Xu B, Zhang QM (2001) Thickness dependence of ferroelectric polarization switching in poly(vinylidene fluoride–trifluoroethylene) spin cast films. *Appl Phys Lett* 78:1122–1124
10. Urayama K, Tsuji M, Neher D (2000) Layer-thinning effects on ferroelectricity and the ferroelectric to paraelectric phase transition of vinylidene fluoride trifluoroethylene copolymer layers. *Macromolecules* 33:8269–8279
11. Xia F, Zhang QM (2004) Schottky emission at the metal polymer interface and its effect on the polarization switching of ferroelectric poly(vinylidene fluoride–trifluoroethylene) copolymer thin films. *Appl Phys Lett* 85(10):1719–1721
12. Choudhuri JR, Vanzo D, Madden PA, Salanne M, Bratko D, Luzar A (2016) Dynamic response in nanoelectrowetting on a dielectric. *ACS Nano* 10:8536–8544
13. Schneemilch M, Welters WJJ, Hayes RA, Ralston J (2000) Electrically induced changes in dynamic wettability. *Langmuir* 16:2924–2927
14. Gersappe D (2002) Molecular mechanisms of failure in polymer nanocomposites. *Phys Rev Lett* 89:058301–058311
15. Puente Orench I, Ania F, Baer E, Hiltner A, Bernal T, Baltá Calleja FJ (2004) Basic aspects of microindentation in multilayered poly (ethylene terephthalate)/polycarbonate films. *Philos Mag* 84(18):1841–1852
16. Baltá-Calleja FJ, Cagliao ME, Adhikari R, Michler GH (2004) Relating microhardness to morphology in styrene/butadiene block copolymer/polystyrene blends. *Polymer* 45(1):247–254
17. Henning S, Michler GH, Ania F, Baltá-Calleja FJ (2005) Microhardness of α - and β -modified isotactic polypropylene at the initial stages of plastic deformation: analysis of micromechanical processes. *Colloid Polym Sci* 283(5):486–495
18. Flores A, Pieruccini M, Stribeck N, Funari SS, Bosch E, Baltá-Calleja FJ (2005) Structure formation in poly (ethylene terephthalate) upon annealing as revealed by microindentation hardness and X-ray scattering. *Polymer* 46(22):9404–9410

19. Ania F, Broza G, Mina MF, Schulte K, Roslaniec Z, Balta-Calleja FJ (2006) Micromechanical properties of poly (butylene terephthalate) nanocomposites with single- and multi-walled carbon nanotubes. *Compos Interfac* 13(1):33–45
20. Flores A, Mathot VBF, Michler GH, Adhikari R, Balta-Calleja FJ (2006) Novel aspects of microindentation hardness in very low crystallinity ethylene-1-octene copolymers: a model for deformation. *Polymer* 47(15):5602–9
21. Uchiyama T, Suyama M, Alam MM, Asano T, Henning S, Flores A, Mina MF (2007) Layer structure formation in oriented poly (ethylene terephthalate) relating to micromechanical properties. *Polymer* 48(2):542–555
22. Shahdad SA, McCabe JF, Bull S, Rusby S, Wassell RW (2007) Hardness measured with traditional Vickers and Martens hardness methods. *Dent Mater* 23(9):1079–1085
23. Bembey AK, Oyen ML, Bushby AJ, Boyde A (2006) Viscoelastic properties of bone as a function of hydration state determined by nanoindentation. *Philos Mag* 86:5691–5703
24. Godara A, Raabe D, Green S (2007) The influence of sterilization processes on the micromechanical properties of carbon fiber-reinforced PEEK composites for bone implant applications. *Acta Biomater* 3(2):209–220
25. Liu Y, Wang M (2007) Fabrication and characteristics of hydroxyapatite reinforced polypropylene as a bone analogue biomaterial. *J Appl Polym Sci* 106(4):2780–2790
26. Vaziri A, Lee H, Mofrad MK (2006) Deformation of the cell nucleus under indentation: mechanics and mechanisms. *J Mater Res* 21(8):2126–2135
27. Kaufman JD, Miller GJ, Morgan EF, Klapperich CM (2008) Time-dependent mechanical characterization of poly (2-hydroxyethyl methacrylate) hydrogels using nanoindentation and unconfined compression. *J Mater Res* 23(5):1472–1481
28. Lu HB, Huang G, Wang B, Mamedov A, Gupta S (2006) Characterization of the linear viscoelastic behavior of single-wall carbon nanotube/polyelectrolyte multilayer nanocomposite film using nanoindentation. *Thin Solid Film* 500(2):197–202
29. Owens FJ (2006) Raman and mechanical properties measurements of single walled carbon nanotube composites of polyisobutylene. *J Mater Chem* 16(5):505–508
30. Chiu WM, Chang YA, Kuo HY, Lin MH, Wen HC (2008) A study of carbon nanotubes/biodegradable plastic polylactic acid composites. *J Appl Polym Sci* 108(5):3024–3030
31. Liu T, Phang IY, Shen L, Chow SY, Zhang WD (2004) Morphology and mechanical properties of multiwalled carbon nanotubes reinforced nylon-6 composites. *Macromolecules* 37(19):7214–7222
32. Chavarria F, Paul DR (2006) Morphology and properties of thermoplastic polyurethane nanocomposites: effect of organoclay structure. *Polymer* 47(22):7760–7773
33. Shen Lu, In YP, Tianxi L, Kaiyang Z (2004) Nanoindentation and morphological studies on nylon 66/organoclay nanocomposites II effect of strain rate. *Polymer* 45(24):8221–8229
34. Wornyo E, Gall K, Yang F, King W (2007) Nanoindentation of shape memory polymer networks. *Polymer* 48(11):3213–3225
35. Chen CH, Sun YY (2006) Mechanical properties of blocked polyurethane/epoxy interpenetrating polymer networks. *J Appl Polym Sci* 101(3):1826–1832
36. Flores A, Pietkiewicz D, Striebeck N, Roslaniec Z, Baltá Calleja FJ (2001) Structural features of random polyester: amide copolymers as revealed by X-ray scattering and microindentation hardness. *Macromolecules* 34(23):8094–8100
37. Marsh DM (1964) Alan Howard cottrell plastic flow in glass. *Proc R Soc Lond* A279420–435
38. Hirst W, Howse MGJW (1969) The indentation of materials by wedges. *Proc R Soc Lond Math Phys Sci* 311(1506):429–444
39. Mir SH, Ochiai B (2016a) Development of hierarchical polymer@Pd nanowire-network: synthesis and application as highly active recyclable catalyst and printable conductive ink. *Chem Open* 5(3):213–218
40. Mir SH, Ochiai B (2017) One-pot fabrication of hollow polymer@Ag nanospheres for printable translucent conductive coatings. *Adv Mater Interfaces* 4(14):1601198
41. Theophile N, Jeong HK (2017) Electrochemical properties of poly (vinyl alcohol) and graphene oxide composite for supercapacitor applications. *Chem Phys Lett* 669:125–129
42. Parrey KA, Aziz A, Ansari SG, Mir SH, Khosla A, Niazi A (2018) Synthesis and characterization of an efficient hole-conductor free halide perovskite $\text{CH}_3\text{NH}_3\text{PbI}_3$ semiconductor absorber based photovoltaic device for IOT. *J Electrochem Soc* 165(8):3023–3029

43. Mir SH, Nagahara LA, Thundat T, Mokarian-Tabari P, Furukawa H, Khosla A (2018) Review: organic-inorganic hybrid functional materials—an integrated platform for applied technologies. *J Electrochem Soc* 165(8):3137–3156
44. Morozov SV, Novoselov KS, Katsnelson MI (2008) Giant intrinsic carrier mobilities in graphene and its bilayer. *Phy Rev Lett* 100:016602
45. Hirata M, Gotou T, Horiuchi S, Fujiwara M, Ohba M (2004) Thin-film particles of graphite oxide I: high-yield synthesis and flexibility of the particles. *Carbon* 42(14):2929–2937
46. Habte AT, Ayele DW (2019) Synthesis and characterization of reduced graphene oxide (rGO) started from graphene oxide (GO) using the tour method with different parameters. *Adv Mater Sci Eng* 5:1–9
47. Ali A, Al-Enizi AM, M, Ali AM, Alamgir K, (2016) Influence of graphene oxide on mechanical, morphological, barrier, and electrical properties of polymer membranes. *Arab J Chem* 9(2):274–286
48. Mir SH, Ochiai B (2016b) Fabrication of polymer-Ag honeycomb hybrid film by metal complexation induced phase separation at the air/water interface. *Macromol Mater Eng* 301(9):1026–1031
49. Sahin O, Uzun O, Kölemen U, Uçar N (2007) Dynamic hardness and reduced modulus determination on the (001) face of B-Sn single crystals by a depth sensing indentation technique. *J Phys Condens Matter* 19:306001
50. Sangwal K, Surowska B, Blaziak P (2002) Analysis of the indentation size effect in the microhardness measurement of some cobalt-based alloys. *Mater Chem Phys* 77:511
51. Graaf DD, Braciszewicz M, Hintzen HT, Sopicka-Lizer M, De WG (2004) The influence of the composition on (the load-dependence of) the microhardness of Y–;Si–;Al–;O–;N glasses as measured by Vickers indentation. *J Mater Sci* 39:2145
52. Lopesa ESN, Cremascoa A, Afonso CRM, Caram R (2011) Effects of double aging heat treatment on the microstructure, vickers hardness and elastic modulus of Ti–Nb alloys. *Mater Charact* 62:673–680
53. Tosun M, Ataoglu S, Arda L, Ozturk O, Asikuzun E, Akcan D, Cakiroglu O (2014) Structural and mechanical properties of ZnMgO nanoparticles. *Mater Sci Eng* 590:416–422
54. Ozturk O, Cetinkara HA, Asikuzun E, Akdogan M, Yilmazlar M, Terzioğlu C (2011) Investigation of mechanical and superconducting properties of iron diffusion-doped Bi-2223 superconductors. *J Mater Sci Mater Electron* 22(9):1501–1508
55. Arda L, Ozturk O, Asikuzun E, Ataoglu S (2013) Structural and mechanical properties of transition metals doped ZnMgO nanoparticles. *J Powder Technol* 235:479–484
56. Cote LJ, Kim F, Huang J (2009) Langmuir-Blodgett assembly of graphite oxide single layers. *J Am Chem Soc* 131:1043–1049
57. Wang H, Hao Q, Yang X, Lu L, Wang X (2010) Effect of graphene oxide on the properties of its composite with polyaniline. *ACS Appl Mater Interfaces* 2(3):821–828
58. Konwer S, Guha AK, Dolui SK (2012) Graphene oxide-filled conducting polyaniline composites as methanol-sensing materials. *J Mater Sci* 48(4):1729–1739
59. Hermann J, DiStasio RA, Tkatchenko A (2017) First-principles models for van der waals interactions in molecules and materials: concepts, theory, and applications. *Chem Rev* 117(6):4714–4758
60. Gregorio R, Captao RC (2000) Morphology and phase transition of high melt temperature crystallized poly(vinylidene fluoride). *J Mater Sci* 35:299–306
61. Elashmawi I, Hakeem N (2008) Effect of PMMA addition on characterization and morphology of PVDF. *Polym Eng Sci* 48(5):895–901
62. Coleman MM, Painter PC (1995) Hydrogen bonded polymer blends. *Prog Polym Sci* 1:20
63. Mao D, Bruce EG, Manuel A, Quevedo L (2011) Ferroelectric Properties and Polarization Switching Kinetic of Poly (vinylidene fluoride-trifluoroethylene) Copolymer. *Ferroelectr Phys Effe* 4:644–654
64. Singh PK, Gaur MS (2018) Enhancement of β -phase of P (VDF–TrFE) 60/40 by BaTiO₃ nano-filler. *Ferroelectrics* 524(1):37–43
65. Martins P, Lopes AC, Lanceros-Mendez S (2014) Electroactive phases of poly(vinylidene fluoride): Determination, processing and applications. *Prog Polym Sci* 39(4):683–706
66. Martins P, Lopes A, Lanceros-Mendez S (2013) Electroactive phases of poly(vinylidene fluoride): determination, processing and applications. *Prog Polym Sci* 39:683–706
67. Liu ZD, Feng Y, Li WL (2015) High dielectric constant and low loss of polymeric dielectric composites filled by carbon nanotubes adhering BaTiO₃ hybrid particles. *RSC Adv* 5:29017–29021

68. Gupta AS, Sarkar CK (2015) Introduction to nano quantum effect on properties of nanomaterials by Chandan Kumar Ghosh. Springer, Berlin
69. Takagahara T, Takeda K (1992) Theory of the quantum confinement effect on excitons in quantum dots of indirect-gap materials. *Phys Rev B* 46:15578
70. Zaman S, Mansoor M, Abubakar AMM (2016) AFM investigation and optical band gap study of chemically deposited PbS thin films. *IOP Conf Ser Mater Sci Eng* 146:012034–012040
71. Santa-CruzBaltá-Calleja CFJ, Zachmann HG, Stribeck N, Asano T (1991) Relating microhardness of poly (ethylene terephthalate) to microstructure. *J Polym Sci Part B Polym Phys* 29:819–824
72. Cagiao ME, ConnorBaltá-Calleja MFJ, Seferis JC (1999) Structure development in a thermoplastic polyimide: cold crystallization as revealed by microhardness. *Polym J* 31(9):739–746
73. Rueda DR, Viksne A, Malers L, Baltá-Calleja FJ, Zachmann HG (1994) Influence of morphology on the microhardness of poly(ethylene naphthalene-2,6-dicarboxylate. *Macromol Chem Phys* 195:3869–3876
74. Kajaks J, Flores A, García-Gutiérrez MC, Rueda DR, Baltá-Calleja FJ (2000) Crystallization kinetics of poly(ethylene naphthalene-2,6-dicarboxylate) as revealed by microhardness. *Polymer* 41(21):7769–7772
75. Baltá-Calleja FJ, Santa Cruz C, Asano T (1993) Physical transitions and crystallization phenomena in poly(ethylene terephthalate) studied by microhardness. *J Polym Sci Part B Polym Phys* 31:557–565
76. Baltá-Calleja FJ, Flores A, Ania F, Michler GH, Baltá-Calleja FJ (eds) (2005) Mechanical properties of polymers based on nanostructure and morphology, 1st edn. Taylor and Francis, Boca Raton (Florida), p 784
77. Baltá-Calleja FJ (2000) Structure-microhardness correlation of polymers and blends. In: Cunha AM, Fakirov S (eds) Structure development during polymer processing: NATO science series. Kluwer Academic Publishers, Dordrecht, pp 145–162
78. Jiang X, Bin Y, Matsuo M (2005) Electrical and mechanical properties of polyimide carbon nanotubes composites fabricated by in situ polymerization. *Polymer* 46:7418–7424
79. Meincke O, Kaempfer D, Weickmann H, Friedrich C, Vathauer M, Warth H (2004) Mechanical properties and electrical conductivity of carbon-nanotube filled polyimide-6and its blends with acrylonitrile/butadiene/styrene. *Polymer* 45:739–748
80. Luo J, Chen S, Li Q, Liu C, Gao S, Zhang J, Guo J (2019) Influence of graphene oxide on the mechanical properties, fracture toughness, and microhardness of recycled concrete. *Nanomaterials* 9(3):325–335
81. Gaur A, Rana D, Maiti P (2019) Mechanical and wear behaviour of poly (vinylidene fluoride)/clay nanocomposite. *J Mater Res Technol* 8(6):5874–5881
82. Smith WF (1996) Principles of materials science and engineering, potential energy curves and material properties, 3rd edn. McGraw-Hill, Columbus
83. Oliver WC, Pharr GM (1992) An improved technique for determining hardness and elastic modulus using load and displacement sensing indentation experiments. *J Mater Res* 7:1564–1583
84. Lin I, Chen CT, BdiKin I, Ball V, Gracio J, Buehler MJ (2014) Tuning heterogeneous poly(dopamine) structures and mechanics: in silico covalent cross-linking and thin film nanoindentation. *Sof Matter* 10:457–464
85. Kariper IA (2015) Hardness of Mn2V2O7 thin films and its influential factors. *Int J Miner Metall Mater* 22:987–991
86. Kariper IA (2016) Hardness of thin films and the influential factors, chapter 1. *Diamond and Carbon Composites and Nanocomposites* 1–20.
87. José AC, Maria CP (2019) Monitoring Dispersion and Re-agglomeration Phenomena during the Manufacture of Polymer Nano composites. *Processi of Poly Nano* 12(1):97–120
88. Fornes TD, Paul DR (2003) Crystallization behavior of nylon 6 nanocomposites. *Polymer* 44(14):3945–3961
89. Cahoon JR, Broughton WH, Kutzak AK (1971) The determination of yield strength from hardness measurements. *Metall Trans* 2:1979–1983
90. Pavlina EJ, Van Tyne CJ (2008) Correlation of yield strength and tensile strength with hardness for steels. *Int J Miner Metall Mater* 17(6):888–893
91. Haihe S, Sijia Y, Shulin S, Huixuan Z (2013) Effect of Miscibility and Crystallization on the Mechanical Properties and Transparency of PVDF/PMMA Blends. *Polym Plast Technol Eng* 52:221–227

92. Ionita M, Pandele AM, Crica L, Pilan L (2014) Improving the thermal and mechanical properties of polysulfone by incorporation of graphene oxide. *Compos Part B* 59:133–139
93. Eggedi O, Valiyaneerilakka U, Dar MR, Varghese S (2014) Nanoindentation and thermal characterization of poly(vinylidene fluoride)/MWCNT nanocomposites. *AIP Adv* 4:047102
94. Shrungi M, Goswami A, Bajpai J, Bajpai AK (2019) Designing kaolin-reinforced bionanocomposites of poly(vinyl alcohol)/gelatin and study of their mechanical and water vapor transmission behavior. *Polym Bull* 76(11):5791–5811
95. Skinner FK, Rotenberg Y, Neumann AW (1989) Contact angle measurements from the contact diameter of sessile drops by means of a modified axisymmetric drop shape analysis. *J Colloid Interface Sci* 130(1):25–34
96. Thabet A, Ebnalwaled AA (2017) Improvement of surface energy properties of PVC nanocomposites for enhancing electrical applications. *Measurement* 110:78–83
97. Ma W, Zhang J, Wang X, Wang S (2007) Effect of PMMA on crystallization behavior and hydrophilicity of poly(vinylidene fluoride)/poly(methyl methacrylate) blend prepared in semi-dilute solutions. *Appl Surf Sci* 253(20):8377–8388
98. Owens DK, Wendt RC (1969) Estimation of the surface free energy of polymers. *J Appl Polym Sci* 13:1741–1747
99. Sagar R, Gaur MS, Bhadoria B (2018) SInvestigation of TSDC and dielectric modulus of PVDF+BaZrO₃ nanocomposites thin film. *Vacuum* 156:375–383
100. Kumar P, Kumar A, Cho KY (2017) An asymmetric electrically conducting self-aligned graphene/polymer composite thin film for efficient electromagnetic interference shielding. *AIP Adv* 7:15103
101. Narayan R, Kim JE, Kim JY (2016) Graphene oxide liquid crystals: discovery, evolution and applications. *Adv Mater* 28:3045–3068
102. Alateyah AI, Dhakal HN, Zhang ZY (2013) Processing, properties, and applications of polymer nanocomposites based on layer silicates: a review. *Adv Polym Technol* 32(4):212–216

Publisher's Note Springer Nature remains neutral with regard to jurisdictional claims in published maps and institutional affiliations.